# Continuous tracking of aortic aneurysm diameter with photoplethysmography: demonstrating feasibility through computational approaches

**Kiran Bhattacharyya** KIRAN.BHATTACHARYYA@SKA-LABS.COM
*SKA Labs, LLC., USA*

## Abstract

Abdominal aortic aneurysms (AAA) affect more than 1% of adults over 50 and carry significant mortality risk. Current surveillance relies on intermittent imaging (ultrasound or MRI) at 6–24 month intervals, which may miss rapid growth acceleration between visits. We investigate the feasibility of continuous aneurysm diameter tracking using photoplethysmography (PPG) signals. Using a one-dimensional hemodynamic model that simulates pulse wave propagation from the heart to the digital artery, we demonstrate that while single-observation diameter estimation is fundamentally limited by noise and confounding variables, aggregating thousands of observations over one or more days may achieve sub-millimeter precision. Specifically, the lower bound error analysis shows diameter uncertainty decreases to 0.7 mm with 1,600 measurements under baseline noise conditions. We validate this approach through 12-month tracking simulations of eight virtual patients with constant and accelerating growth rates, achieving root-mean-square tracking errors of ∼0.3 mm. Furthermore, we demonstrate that patient-specific model calibration from clinical measurements, despite yielding imperfect parameter estimates, still enables accurate diameter tracking (median RMSE = 0.49 mm across 50 virtual patients). These results suggest that wearable PPG monitoring could complement traditional imaging for aneurysm surveillance, potentially enabling earlier detection of growth acceleration and more timely clinical intervention.

**Data and Code Availability** All data produced in the present study and code for generating said data are available upon reasonable request to the authors.

**Institutional Review Board (IRB)** This research does not require IRB approval since it is not "human subjects research" as it does not include activities that involve interaction with individuals or access to identifiable private information.

## 1. Introduction

Aortic aneurysms represent a significant public health burden, with abdominal aortic aneurysms (AAA) affecting 4–8% of men and 0.5–1.5% of women over age 65 (Kent et al., 2014). These pathological dilations of the aortic wall can remain asymptomatic before sudden rupture, which carries high mortality rates (Reimerink et al., 2013). Current clinical practice manages aneurysms through periodic imaging surveillance. Guidelines recommend surgery when aneurysm diameter ≥55 mm or when growth rate ≥5 $\frac{\text{mm}}{\text{year}}$ (Elefteriades, 2008). However, imaging is typically performed at 6–24 month intervals using computed tomography (CT), magnetic resonance imaging (MRI), or ultrasound. Beyond the logistics burden, this intermittent monitoring presents limitations. First, aneurysms can transition to rapidly expanding growth patterns between imaging appointments, potentially rupturing before the next scan. Second, growth rates are under-estimated by averaging across long intervals that obscure recent accelerations in growth.

These limitations motivate investigation of continuous monitoring approaches that could complement traditional imaging. An ideal technology would provide frequent, non-invasive measurements of aneurysm size at home, alerting clinicians to unexpected changes while providing reassurance during stable periods.

Photoplethysmography (PPG) has emerged as a ubiquitous sensing modality in wearable devices. PPG signals contain rich information about cardiovascular function beyond oxygen saturation (Elgendi, 2012). Features extracted from the PPG waveform—including pulse transit time, augmentation index,

© 2026 K. Bhattacharyya.

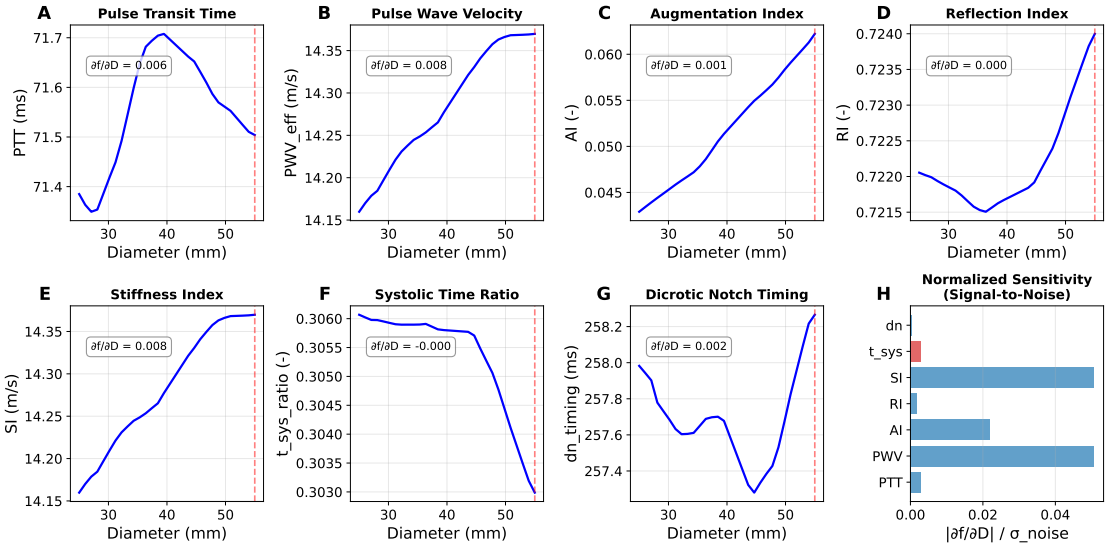


Figure 1: Sensitivity of PPG features to aneurysm diameter. Top row: Pulse transit time, pulse wave velocity, augmentation index, and reflection index versus diameter. Bottom row: Stiffness index, systolic time ratio, dicrotic notch timing, and normalized sensitivity comparison. Vertical dashed lines indicate the 55 mm surgical threshold. Sensitivities ($\partial f/\partial D$) are shown in each panel. The normalized sensitivity panel demonstrates that all features have low signal-to-noise ratios for single-observation diameter estimation.

and reflection index—have been shown to correlate with arterial stiffness, blood pressure, and vascular health (Millasseau et al., 2006; Charlton et al., 2022). An aneurysm creates a region of increased compliance and altered impedance within the arterial tree, modifying pulse wave propagation from the heart to peripheral measurement sites (Sakalihasan et al., 2018). These modifications may manifest as changes in waveform morphology, timing, and reflection characteristics—all potentially detectable in PPG signals recorded at the fingertip or wrist.

In this work, we present a computational proof-of-concept demonstrating the feasibility of tracking aortic aneurysm diameter using continuous PPG monitoring. Our approach combines a reduced-order hemodynamic model with Bayesian sequential estimation to aggregate information from thousands of PPG measurements, exploiting natural physiological variation to resolve the diameter signal from confounding variables. Specifically, we make the following contributions:

1. We characterize the fundamental sensitivity and identifiability limitations of single-observation diameter estimation from PPG features, demonstrating that the problem is severely ill-conditioned.

2. We show theoretically via Cramér-Rao bound analysis that aggregating hundreds to thousands of observations—feasible with continuous wearable monitoring—can reduce diameter uncertainty to sub-millimeter levels.

3. We demonstrate accurate 12-month diameter tracking (RMSE $< 0.35$ mm) for virtual patients with both constant and accelerating growth rates.

4. We evaluate the robustness of the tracking framework to imperfect patient-specific model calibration, showing that clinically acceptable tracking accuracy is maintained despite parameter estimation errors.

### 1.1. Generalizable Insights about Machine Learning in the Context of Healthcare

This work offers insights extending beyond aortic aneurysm monitoring to broader challenges in wearable-based health sensing:

- **Physics-based models enable rigorous feasibility analysis before clinical studies.** Rather than collecting clinical data and retrospectively asking whether a signal exists, we demonstrate a forward approach: using a physiologically-grounded computational model to derive theoretical bounds (Cramér-Rao), characterize identifiability (condition number analysis), and simulate realistic noise scenarios. This *in silico* methodology allows us to determine *why* a measurement should be possible, *under what conditions* it will succeed, and *how many observations* are required—questions difficult to answer from empirical data alone. While our simulations cannot capture all real-world complexities, they provide principled guidance for study design and realistic expectations before resource-intensive clinical validation.

- **Temporal aggregation can overcome single-measurement identifiability failures.** A key finding is that the severely ill-conditioned single-observation problem becomes tractable through massive temporal aggregation exploiting natural physiological variation. This principle—that wearable devices can accumulate statistical power over time to resolve signals invisible in any individual measurement—may apply to other "needle-in-a-haystack" biomarker detection problems where the target signal is confounded by faster-varying physiological states that can be represented through physical models.

- **Surrogate models bridge mechanistic understanding and scalable inference.** Our neural surrogate, trained on physics-based simulations, enables Bayesian inference at scale while preserving interpretability of the underlying hemodynamic model. This hybrid approach—mechanistic models for insight, learned surrogates for computation—offers a template for healthcare applications where both physiological grounding and computational tractability are required.

We emphasize that all results presented are computational; the true test of this framework requires prospective clinical validation correlating PPG-derived estimates with imaging-confirmed diameter measurements. The gap between idealized simulations and real-world signal quality, patient heterogeneity, and device variability remains substantial. Nonetheless, this work establishes theoretical plausibility and identifies the critical requirements (observation counts, noise tolerances, calibration accuracy) that clinical studies must achieve.

## 2. Methods

We developed a one-dimensional (1D) computational fluid dynamics model to simulate arterial blood flow from the heart to the digital artery, enabling prediction of PPG-derived features as a function of AAA diameter and hemodynamic parameters.

**Governing Equations.** The model solves the 1D Navier-Stokes equations for blood flow in compliant vessels, consisting of conservation of mass and momentum:

$$\frac{\partial A}{\partial t} + \frac{\partial Q}{\partial x} = 0 \tag{1}$$

$$\frac{\partial Q}{\partial t} + \frac{\partial}{\partial x}\left(\alpha \frac{Q^2}{A} + \frac{AP}{\rho}\right) = -\frac{f \cdot Q}{A} \tag{2}$$

where $A(x,t)$ is the vessel cross-sectional area [m$^2$], $Q(x,t)$ is the volumetric flow rate [m$^3$/s], $P(x,t)$ is the transmural pressure [Pa], $\rho = 1060$ kg/m$^3$ is blood density, $\alpha = 1.0$ is the momentum correction coefficient (flat velocity profile), and $f$ represents viscous friction forces.

**Constitutive Relations.** Vessel wall mechanics are described by a nonlinear tube law relating pressure to area:

$$P(x,t) = P_{\text{ext}} + \beta(x)\left(\sqrt{A(x,t)} - \sqrt{A_0(x)}\right) \tag{3}$$

where $P_{\text{ext}} = 0$ Pa is external pressure, $A_0(x)$ is the reference cross-sectional area at zero transmural pressure, and $\beta(x)$ [Pa $\cdot$ m] is the wall stiffness parameter. The local pulse wave velocity is:

$$c(x) = \sqrt{\frac{\beta(x)}{2\rho}} A(x)^{1/4} \tag{4}$$

Viscous friction follows a Poiseuille-like profile:

$$S_{\text{friction}} = -\frac{22\pi\mu Q}{\rho A} \tag{5}$$

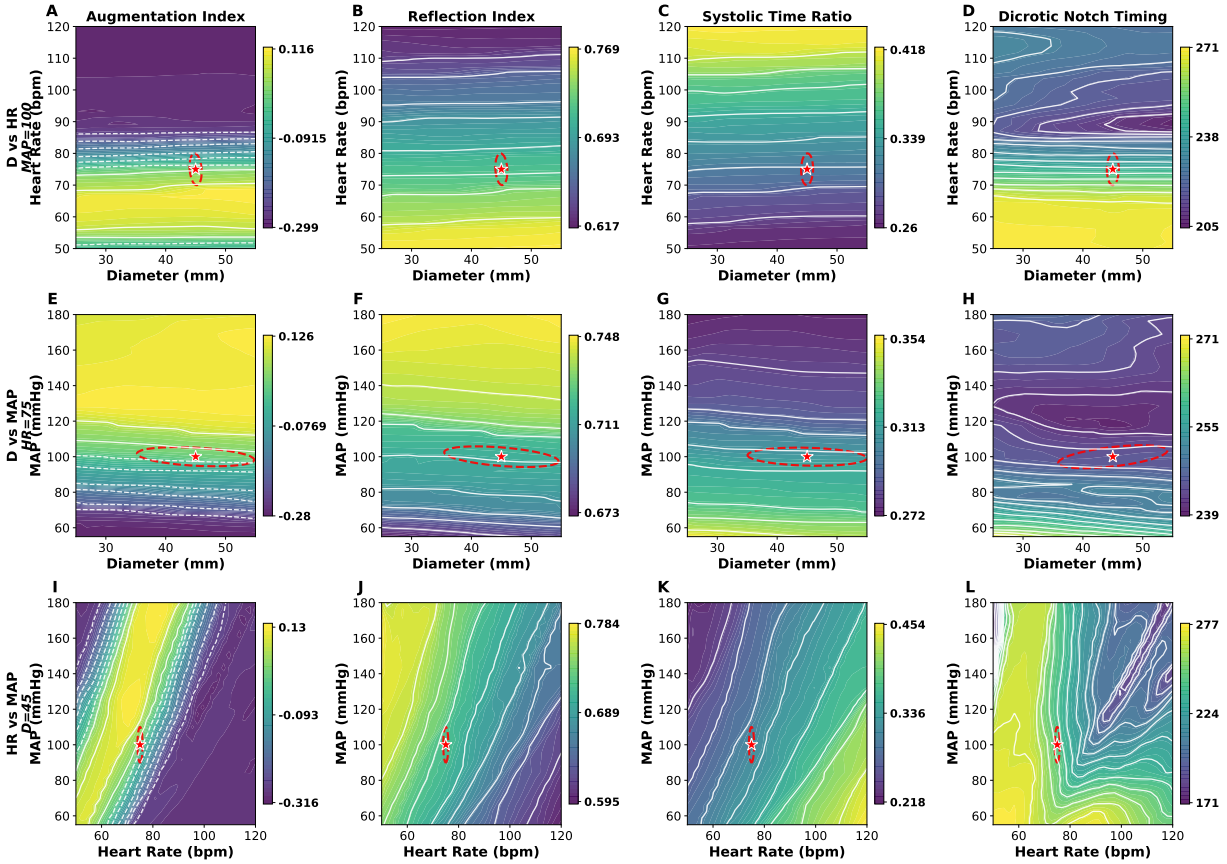


Figure 2: Feature space structure and measurement uncertainty propagation. Rows show cross-sections of the 3D parameter space: diameter vs. heart rate (top), diameter vs. MAP (middle), and heart rate vs. MAP (bottom). Columns correspond to four PPG-only features. Red stars indicate the nominal operating point (D=45 mm, HR=75 bpm, MAP=100 mmHg). Red dashed ellipses show $2\sigma$ uncertainty regions from HR (heart) and MAP (mean arterial pressure) measurement errors. The elongated ellipses along diameter axes indicate poor single-observation identifiability (condition number $\kappa \approx 740$).

where $\mu = 0.004$ Pa · s is blood dynamic viscosity.

**Arterial Geometry and Aneurysm Modeling.** The computational domain spans $L = 1.0$ m from the proximal aorta to the digital artery, discretized with spatial step $\Delta x = 0.01$ m. The baseline geometry features exponential tapering from proximal radius $r_0^{\text{prox}} = 32$ mm to distal radius $r_0^{\text{dist}} = 1.5$ mm:

$$r_0(x) = r_0^{\text{prox}} \exp\left(-\frac{\ln(r_0^{\text{prox}}/r_0^{\text{dist}})}{L} \cdot x\right) \tag{6}$$

Wall stiffness increases distally to reflect physiological arterial stiffening, ranging from $\beta^{\text{prox}} = 5 \times 10^4$ Pa · m (yielding PWV $\approx 5$ m/s in the aorta) to $\beta^{\text{dist}} = 2 \times 10^6$ Pa · m (PWV $\approx 15$ m/s in digital arteries).

AAA geometry is incorporated via a Gaussian dilation envelope centered at $x = 0.35$ m (abdominal region) with half-width 5 cm. For a specified maximum diameter $D_{\max}$, the local area is modified as:

$$A_0(x) = A_0^{\text{baseline}}(x) \cdot \left[1 + \left(\left(\frac{D_{\max}}{D_{\text{baseline}}}\right)^2 - 1\right) \exp\left(-\frac{(x-0.35)^2}{2(0.05)^2}\right)\right. \tag{7}$$

Aneurysmal wall degradation is modeled as a 40% local reduction in $\beta(x)$ following the same Gaussian envelope, representing increased local compliance.

**Numerical Method.** The system is solved using the Lax-Friedrichs finite difference scheme, chosen for its stability properties. The time step satisfies the Courant-Friedrichs-Lewy (CFL) condition with CFL number 0.4:

$$\Delta t = 0.4 \cdot \frac{\Delta x}{\max_i(c_i + |u_i|)} \tag{8}$$

At the inlet (proximal aorta), a physiologically realistic cardiac flow waveform is prescribed, consisting of rapid systolic ejection (35% of cycle), brief early diastolic backflow representing valve closure, and zero diastolic flow. Stroke volume (baseline 70 mL) is adjusted based on mean arterial pressure (MAP) with sensitivity of $-1\%$ per mmHg deviation from 90 mmHg baseline.

At the outlet (digital artery), a three-element Windkessel model ($R_1$-$C$-$R_2$) represents peripheral impedance, with characteristic impedance $R_1 = 5 \times 10^7$ Pa $\cdot$ s/m$^3$, peripheral resistance $R_2 = 5 \times 10^8$ Pa $\cdot$ s/m$^3$, and compliance $C = 2 \times 10^{-9}$ m$^3$/Pa.

**Feature Extraction.** Each simulation runs for 5 cardiac cycles with the final cycle recorded for analysis. Proximal pressure and distal area (PPG proxy) waveforms are extracted. Seven hemodynamic features are computed: 1) Pulse Transit Time (PTT): Foot-to-foot delay between proximal pressure and distal area waveforms [ms], 2) Effective Pulse Wave Velocity (PWV): $L$/PTT [m/s], 3) Augmentation Index (AI): Derived from diastolic decay rate, reflecting wave reflection, 4) Reflection Index (RI): Ratio of diastolic to total pulse area, 5) Stiffness Index (SI): Approximated as effective PWV [m/s], 6) Systolic Time Ratio: Fraction of cardiac cycle in systole, and 7)Dicrotic Notch Timing: Time from peak to dicrotic notch [ms].

For analyses using PPG alone (without ECG synchronization), we restrict to the four features computable from the PPG waveform independently: augmentation index, reflection index, systolic time ratio, and dicrotic notch timing.

### 2.1. Sensitivity Analysis

To quantify the sensitivity of PPG features to aneurysm diameter, we computed each feature across a physiologically relevant diameter range (25–55 mm) while holding heart rate (70 bpm) and MAP (95 mmHg) constant. For each feature $f$, we calculated the sensitivity $\partial f/\partial D$ using linear regression over the diameter range. To assess signal-to-noise ratio, we normalized each sensitivity by the corresponding measurement noise standard deviation $\sigma_{\text{noise}}$: PTT ($\sigma = 2.0$ ms), PWV ($\sigma = 0.15$ m/s), AI ($\sigma = 0.03$), RI ($\sigma = 0.03$), SI ($\sigma = 0.15$ m/s), systolic time ratio ($\sigma = 0.03$), and dicrotic notch timing ($\sigma = 5.0$ ms). The normalized sensitivity $|\partial f/\partial D|/\sigma_{\text{noise}}$ quantifies how many standard deviations of noise correspond to a 1 mm change in diameter.

### 2.2. Measurement Uncertainty Propagation and Identifiability Analysis

We generated three-dimensional feature maps by systematically varying diameter (25–55 mm), heart rate (HR, 50–120 bpm), and mean arterial pressure (MAP, 55–180 mmHg) for the four PPG-only features. The feature space was visualized as two-dimensional cross-sections at fixed values of the third parameter.

To quantify measurement uncertainty propagation, we computed $2\sigma$ uncertainty ellipses centered at a nominal measurement point ($D = 45$ mm, HR = 75 bpm, MAP = 100 mmHg) with realistic measurement uncertainties ($\sigma_{\text{HR}} = 1$ bpm, $\sigma_{\text{MAP}} = 10$ mmHg, Appendix C). Ellipse orientation and eccentricity were determined by local feature gradients.

We performed Jacobian analysis to assess parameter identifiability. The Jacobian matrix $\mathbf{J}$ (4 features $\times$ 3 parameters) was computed using finite differences. Each row was normalized by measurement noise and columns scaled by physiological parameter ranges ($\pm 15$ mm for diameter, $\pm 25$ bpm for HR, $\pm 25$ mmHg for MAP). The condition number $\kappa(\mathbf{J})$ quantifies parameter correlation: $\kappa < 10$ indicates excellent identifiability, $10 \leq \kappa < 100$ moderate identifiability, $100 \leq \kappa < 1000$ poor identifiability, and $\kappa \geq 1000$ very poor identifiability.

### 2.3. Cramér-Rao Bound Analysis

We computed the Cramér-Rao lower bound (CRLB) for diameter estimation assuming fixed true diameter with varying physiological state. The Fisher information for diameter was calculated as:

$$I_D = \sum_i \sum_j \frac{(\partial f_j/\partial D)^2}{\sigma^2_{\text{total},j}} \tag{9}$$

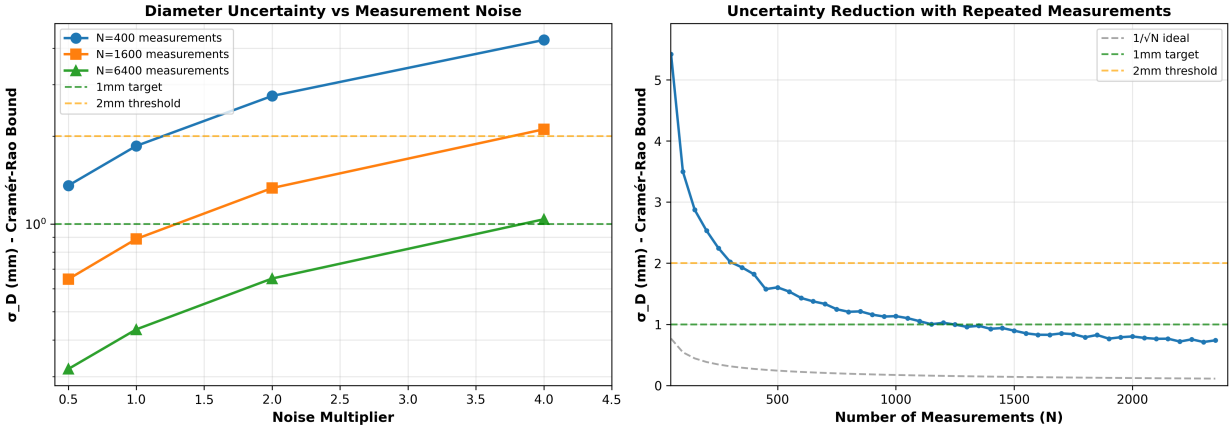


Figure 3: Cramér-Rao lower bounds for diameter estimation. Left: Diameter uncertainty versus noise multiplier for different measurement counts. The 1 mm target (green dashed) and 2 mm clinical threshold (orange dashed) are shown for reference. Right: Uncertainty reduction with increasing measurements at baseline noise, compared to ideal $1/\sqrt{N}$ scaling. Sub-millimeter precision is theoretically achievable with 1,600+ measurements.

where the sum over $i$ represents multiple measurements with different HR and MAP values, the sum over $j$ represents the PPG-only features, and $\sigma^2_{\text{total},j}$ accounts for both intrinsic feature noise and propagated uncertainty from HR/MAP measurements:

$$\sigma^2_{\text{total},j} = \sigma^2_{\text{feature},j} + \left(\frac{\partial f_j}{\partial \text{HR}}\right)^2 \sigma^2_{\text{HR}} + \left(\frac{\partial f_j}{\partial \text{MAP}}\right)^2 \sigma^2_{\text{MAP}} \tag{10}$$

The CRLB on diameter uncertainty is $\sigma_D \geq 1/\sqrt{I_D}$.

We tested four noise multipliers (0.5×, 1×, 2×, 4×) applied to baseline uncertainties ($\sigma_{\text{HR}} = 1$ bpm, $\sigma_{\text{MAP}} = 10$ mmHg) and three measurement counts ($N = 400$, 1600, 6400 observations). For each measurement, HR was sampled uniformly from [60, 90] bpm and MAP from [80, 110] mmHg.

### 2.4. Neural Surrogate Model

To enable computationally tractable inverse problems, we developed a neural network surrogate approximating the 1D Navier-Stokes solver.

The surrogate is a fully connected multilayer perceptron (MLP) with 11-dimensional input comprising: aneurysm diameter $D$ (mm), heart rate HR (bpm), MAP (mmHg), vessel length $L$ (m), proximal resistance $R_1$ ($\text{Pa} \cdot \text{s/m}^3$), distal resistance $R_2$ ($\text{Pa} \cdot \text{s/m}^3$), Windkessel compliance $C_{\text{wk}}$ ($\text{m}^3/\text{Pa}$), proximal radius $r_0^{\text{prox}}$ (m), distal radius $r_0^{\text{dist}}$ (m), proximal stiffness $\beta^{\text{prox}}$ (Pa), and distal stiffness $\beta^{\text{dist}}$ (Pa). The network has three hidden layers with [128, 128, 64] neurons using ReLU activations and dropout ($p = 0.1$). The 7-dimensional output predicts PTT, $\text{PWV}_{\text{eff}}$, AI, RI, SI, systolic time ratio, and dicrotic notch timing. The network contains approximately 30,000 trainable parameters.

Training data was generated using Latin Hypercube Sampling over the 11-dimensional parameter space, with 40,000 samples for models where parameter ranges were representative of the population. The network was trained with Adam optimizer (learning rate $\alpha = 0.001$), MSE loss, batch size 64, and early stopping (patience 10 epochs) monitoring validation loss.

On held-out validation sets, the surrogate achieved $R^2 > 0.88$ for all features, with relative errors $< 5\%$ for most features. The surrogate provides approximately 1000× speedup compared to the numerical solver.

### 2.5. Bayesian Sequential Diameter Tracking

We implemented a Bayesian tracking framework that fuses biomechanical growth model priors with PPG-based diameter observations.

The prior distribution at time $t$ is computed from the posterior at $t - \Delta t$ propagated forward:

$$D_{\text{prior}}(t) = D_{\text{post}}(t - \Delta t) + \hat{r}_{\text{growth}} \times \Delta t \tag{11}$$

$$\sigma^2_{\text{prior}}(t) = \sigma^2_{\text{post}}(t - \Delta t) + \sigma^2_{\text{growth}} \times \Delta t^2 \tag{12}$$

where $\hat{r}_{\text{growth}}$ is the adaptively estimated growth rate and $\sigma_{\text{growth}} = 0.3$ mm/month represents growth model uncertainty.

At each timepoint, synthetic PPG measurements are generated by computing true PPG features from true diameter, true HR, and true MAP and adding Gaussian noise to all. Then inverting using joint optimization over diameter, HR, and MAP with the SLSQP algorithm and neural surrogate. Observation uncertainty was set to $\sigma_{\text{PPG}} = 1.0$ mm. Essentially, we infer the diameter, HR, and MAP that best explain the PPG features given other

The posterior distribution is obtained via Bayesian fusion:

$$\sigma^2_{\text{post}} = \frac{1}{1/\sigma^2_{\text{prior}} + 1/\sigma^2_{\text{PPG}}} \tag{13}$$

$$D_{\text{post}} = \sigma^2_{\text{post}} \left( \frac{D_{\text{prior}}}{\sigma^2_{\text{prior}}} + \frac{D_{\text{PPG}}}{\sigma^2_{\text{PPG}}} \right) \tag{14}$$

The growth rate estimate is updated using exponential moving average with learning rate $\alpha = 0.3$:

$$\begin{aligned} \hat{r}_{\text{growth}}(t) &= (1 - \alpha) \times \hat{r}_{\text{growth}}(t - \Delta t) \\ &+ \alpha \times \frac{D_{\text{PPG}} - D_{\text{post}}(t - \Delta t)}{\Delta t} \end{aligned} \tag{15}$$

### 2.6. Tracking Simulation Protocol

We simulated eight virtual patients over 12 months with four measurements per month (48 total). The cohort included four patients with constant growth rates (initial diameters 30, 35, 40, 45 mm with growth rates 0.1, 0.1, 0.2, 0.5 mm/month) and four with accelerating growth (same initial diameters, zero growth for months 0–6, then matching rates for months 6–12).

Each measurement comprised 3,200 observations generated by the forward model with varying HR (sampled from [60, 90] bpm), MAP (sampled from [80, 110] mmHg), and other parameters $(L, R_1, R_2, C_{\text{wk}}, r_0^{\text{prox}}, r_0^{\text{dist}}, \beta^{\text{prox}}, \beta^{\text{dist}})$ vary within physiological bounds for a given individual. Each observation (HR, MAP, and PPG features) are also adjusted by adding realistic measurement noise. The Bayesian tracker had uncertain knowledge of initial growth rate and no knowledge of future acceleration, relying on HR, MAP, and PPG observations to detect changes.

### 2.7. Patient-Specific Model Calibration

In all previous experiments, we held parameters $(L, R_1, R_2, C_{\text{wk}}, r_0^{\text{prox}}, r_0^{\text{dist}}, \beta^{\text{prox}}, \beta^{\text{dist}})$ in the 1D hemodynamic model to nominal values or varied them by ±15% from the nominal value to represent biological variance within an individual. Here we assess whether tracking remains accurate when these parameters must first be calibrated to an individual.

#### 2.7.1. Stage 1: Parameter Calibration

For 50 fictive patients, we assign parameters $(L, R_1, R_2, C_{\text{wk}}, r_0^{\text{prox}}, r_0^{\text{dist}}, \beta^{\text{prox}}, \beta^{\text{dist}})$ through pseudo-random selection to vary within ±30% of nominal values. Then we estimated these eight physiological parameters from 10 clinical measurements combining accurate diameter, HR, and MAP with noisy PPG features. Calibration minimized the weighted sum of squared residuals:

$$\min_{\boldsymbol{\theta}} \sum_i \sum_j \frac{(f_{\text{obs},ij} - f_{\text{pred},ij}(D_i, \text{HR}_i, \text{MAP}_i, \boldsymbol{\theta}))^2}{\sigma_j^2} \tag{16}$$

where $\boldsymbol{\theta} = [L, R_1, R_2, C_{\text{wk}}, r_0^{\text{prox}}, r_0^{\text{dist}}, \beta^{\text{prox}}, \beta^{\text{dist}}]$ using L-BFGS-B optimization.

#### 2.7.2. Stage 2: Tracking with Calibrated Parameters

For the same 50 fictive patients, we simulated 12-month tracking using calibrated (imperfect) parameters while true diameter evolved according to randomly assigned growth dynamics. The tracking algorithm treated calibrated parameters as ground truth.

Performance was evaluated by comparing estimated to true diameter trajectories using RMSE, MAE, and maximum error. We computed correlations between parameter estimation errors and tracking RMSE to identify which parameters must be accurately calibrated.

## 3. Results

### 3.1. Model Validation

We first validate that the 1D hemodynamic model produces physiologically realistic PPG-like wave-

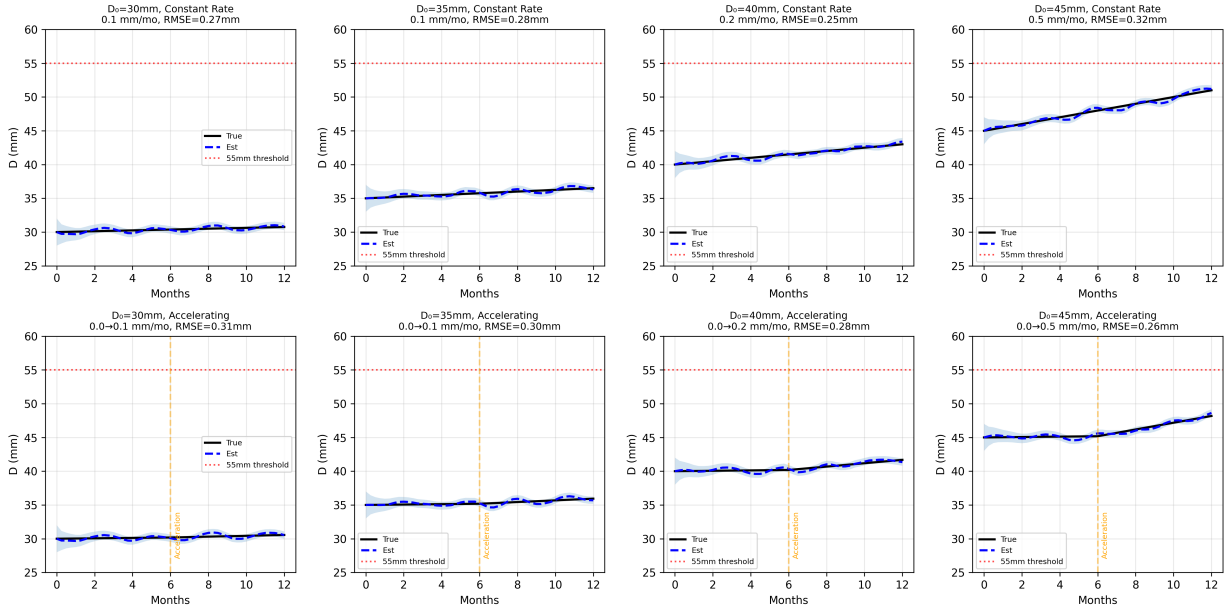


Figure 4: Twelve-month diameter tracking for eight virtual patients. Top row: Constant growth rates (0.1, 0.1, 0.25, 0.5 mm/month for initial diameters 30, 35, 40, 45 mm). Bottom row: Accelerating growth (zero growth months 0–6, then matching rates). Black solid lines: true diameter; blue dashed lines: estimated diameter; blue shading: $\pm 2\sigma$ uncertainty; orange vertical lines: acceleration timepoints; red dotted lines: 55 mm surgical threshold. RMSE values are shown in each panel title.

forms at the digital artery (Appendix A). The simulated waveforms exhibit characteristic features including rapid systolic upstroke, dicrotic notch, and diastolic decay. Varying mean arterial pressure across a wide range (30–200 mmHg) produces expected changes in waveform morphology and amplitude, validating the model's hemodynamic fidelity.

### 3.2. Sensitivity of PPG Features to Aneurysm Diameter

Figure 1 shows the relationship between PPG-derived features and aneurysm diameter across the clinically relevant range (25–55 mm). All features exhibit detectable but modest sensitivity to diameter changes. Pulse wave velocity and stiffness index show monotonically increasing relationships with diameter, while augmentation index and reflection index display more complex, non-monotonic patterns. The normalized sensitivity panel (bottom right) reveals that SI and PWV have the highest signal-to-noise ratios ($|\partial f/\partial D|/\sigma_{\text{noise}} \approx 0.05$), while dicrotic notch timing provides the most informative PPG-only feature.

Critically, these sensitivities are small relative to measurement noise—a 1 mm diameter change produces feature changes of only 0.01–0.05 standard deviations. This fundamental limitation motivates the multi-observation aggregation strategy developed in subsequent sections.

### 3.3. Measurement Uncertainty and Parameter Identifiability

Figure 2 presents the feature space structure and uncertainty propagation analysis. The 3×4 grid of heatmaps reveals that PPG features vary strongly with both HR and MAP, with iso-feature contours often running nearly parallel to diameter axes. This geometry creates fundamental identifiability challenges: a given feature value could correspond to many combinations of diameter, HR, and MAP.

The red dashed ellipses visualize $2\sigma$ uncertainty regions arising from realistic HR ($\pm 1$ bpm) and MAP ($\pm 10$ mmHg) measurement errors. These ellipses span large ranges along the diameter axis, indicating

that physiological state uncertainty dominates diameter estimation uncertainty.

Jacobian analysis yielded a condition number $\kappa \approx 740$, placing the single-observation diameter estimation problem firmly in the "poor identifiability" regime. Singular value decomposition revealed that the maximum-to-minimum singular value ratio reflects strong correlation between diameter and MAP effects on most features.

### 3.4. Cramér-Rao Bounds for Multi-Observation Diameter Estimation

Figure 3 demonstrates how diameter estimation uncertainty decreases with increasing numbers of observations and varies with measurement noise levels. The left panel shows that at baseline noise (1×), uncertainty decreases from approximately 2.8 mm with 400 measurements to 0.7 mm with 6,400 measurements. Even with elevated noise (4×), 6,400 measurements achieve approximately 1.0 mm precision.

The right panel illustrates uncertainty reduction as a function of measurement count at baseline noise. The observed scaling approaches but does not perfectly match the ideal $1/\sqrt{N}$ behavior (gray dashed line), reflecting the additional variance contributed by HR and MAP measurement uncertainty. Nonetheless, the results demonstrate that sub-millimeter precision—adequate for clinical tracking—is theoretically achievable with feasible observation counts. Collecting 1,600 observations (approximately 108 minutes of monitoring at 5 cardiac cycles per observation) brings uncertainty below the 1 mm target threshold.

### 3.5. Longitudinal Diameter Tracking

Figure 4 presents 12-month tracking results for eight virtual patients. The top row shows four patients with constant growth rates; the bottom row shows four patients whose growth accelerated at month 6.

For constant growth patients, the Bayesian tracker maintains close agreement with true diameter throughout the monitoring period, with RMSE ranging from 0.25–0.32 mm and maximum errors below 0.61 mm. The $\pm 2\sigma$ uncertainty bands (blue shading) appropriately capture the true diameter trajectory.

For accelerating growth patients, the tracker successfully detects and adapts to the growth rate change despite having no prior knowledge of the acceleration event. Following the acceleration at month 6 (orange vertical lines), the adaptive growth rate estimator increases $\hat{r}_{\text{growth}}$ within 1–2 measurement cycles, enabling continued accurate tracking. RMSE values (0.26–0.31 mm) remain comparable to the constant growth cases, demonstrating robustness to dynamic growth patterns.

Table 1: Patient-specific parameter calibration performance across 50 virtual patients. Parameters are grouped by identifiability: well-identified ($R^2 > 0.7$), moderately identified ($0.1 < R^2 < 0.7$), and poorly identified ($R^2 < 0.1$).

| Parameter | RMSE | $R^2$ | MAPE (%) |
|---|---|---|---|
| *Well-identified* | | | |
| $L$ | 0.029 m | 0.97 | 1.8 |
| $\beta^{\text{prox}}$ | $1.2 \times 10^4$ Pa | 0.75 | 15.6 |
| $\beta^{\text{dist}}$ | $4.3 \times 10^5$ Pa | 0.78 | 15.3 |
| *Moderately identified* | | | |
| $R_2$ | $2.4 \times 10^8$ Pa · s/m$^3$ | 0.13 | 60.1 |
| *Poorly identified* | | | |
| $R_1$ | $2.3 \times 10^7$ Pa · s/m$^3$ | $< 0.01$ | 44.1 |
| $C_{\text{wk}}$ | $1.3 \times 10^{-9}$ m$^3$/Pa | 0.01 | 8.9 |
| $r_0^{\text{prox}}$ | 2.3 mm | $< 0.01$ | 17.6 |
| $r_0^{\text{dist}}$ | 0.29 mm | $< 0.01$ | 17.6 |

### 3.6. Patient-Specific Calibration Results

Table 1 summarizes parameter estimation performance across 50 virtual patients. The calibration procedure achieved high accuracy for vessel length ($R^2 = 0.97$, MAPE = 1.8%) and arterial stiffness parameters ($R^2 = 0.75$–$0.78$, MAPE $\approx 15\%$). However, Windkessel model parameters ($R_1$, $R_2$, $C_{\text{wk}}$) and vessel radii showed poor identifiability ($R^2 < 0.15$), consistent with theoretical expectations for redundant parameters in this model structure.

### 3.7. Tracking with Imperfectly Calibrated Parameters

Figure 5 shows tracking results for six representative patients using calibrated (imperfect) model parameters. Despite substantial errors in some physiological parameters, tracking accuracy remains clinically acceptable. The estimated diameter trajectories (blue dashed) track the true trajectories (black solid) with typical deviations of 0.5–1.0 mm.

Table 2: Tracking performance summary across 50 virtual patients using imperfectly calibrated parameters.

| Metric | Median | IQR |
|---|---|---|
| RMSE (mm) | 0.49 | [0.35, 0.72] |
| MAE (mm) | 0.38 | [0.27, 0.56] |
| Maximum error (mm) | 1.21 | [0.89, 1.58] |
| Final diameter error (mm) | 0.41 | [0.22, 0.68] |

Table 2 summarizes tracking performance across all 50 virtual patients. Median RMSE was 0.49 mm with interquartile range [0.35, 0.72] mm; median maximum error was 1.21 mm. Only 4% of patients exceeded 1.5 mm RMSE, and none exceeded 2 mm maximum error during stable growth periods.

Table: Correlation analysis between parameter calibration errors and tracking RMSE. This table should show which parameters most critically affect tracking accuracy.

# 4. Discussion

This work demonstrates the theoretical feasibility of tracking aortic aneurysm diameter using continuous PPG monitoring from wearable devices. Our computational approach reveals both fundamental limitations and promising pathways for this novel application.

## 4.1. The Challenge of Single-Observation Estimation

Our sensitivity and identifiability analyses confirm an intuitive concern: detecting small geometric changes in the abdominal aorta from a peripheral measurement site is extraordinarily challenging. The condition number $\kappa \approx 740$ indicates that single PPG measurements cannot reliably distinguish diameter changes from physiological state variations in heart rate and blood pressure. This finding aligns with prior work on pulse wave analysis, which has generally focused on proximal measurements or invasive sensors for aortic characterization (Nichols et al., 2011).

However, this limitation does not preclude clinical utility. The key insight is that wearable devices enable measurement paradigms impossible in clinical settings—specifically, the acquisition of thousands of observations per day under naturally varying physiological conditions.

## 4.2. Exploiting Physiological Variation

The Cramér-Rao bound analysis demonstrates that aggregating observations across the natural range of heart rate and blood pressure effectively "separates" the diameter signal from confounding variables. As HR and MAP vary throughout daily activities, the feature space is sampled along different directions, breaking the degeneracy that plagues single observations. This principle has been applied successfully in other wearable sensing domains, including PPG-based blood pressure estimation (Mukkamala et al., 2015).

The practical implication is that approximately 2–3 hours of cumulative monitoring (1,600 observations at 5 cardiac cycles each) can theoretically achieve sub-millimeter diameter precision. For a wearable device worn continuously, this measurement window could be accumulated over hours to days, with the Bayesian fusion framework weighting observations by their uncertainty.

## 4.3. Robustness to Growth Dynamics

The tracking simulations demonstrate that the Bayesian framework can detect and adapt to growth rate changes without explicit knowledge of acceleration events. This capability is clinically significant because sudden growth acceleration is precisely the scenario where continuous monitoring could provide the greatest benefit relative to intermittent imaging (Thompson et al., 2002).

The adaptive growth rate estimator, while simple (exponential moving average), proves sufficient to track the simulated growth patterns. More sophisticated approaches—such as change-point detection or growth model switching—could potentially improve response to abrupt transitions.

## 4.4. Calibration and Practical Identifiability

The calibration results reveal a nuanced picture of parameter identifiability. While several parameters (vessel length, arterial stiffness) can be estimated with reasonable accuracy from clinical measurements, others (Windkessel parameters, vessel radii) remain practically unidentifiable. This finding is consistent with theoretical analyses of inverse problems in cardiovascular modeling (Banks et al., 2014).

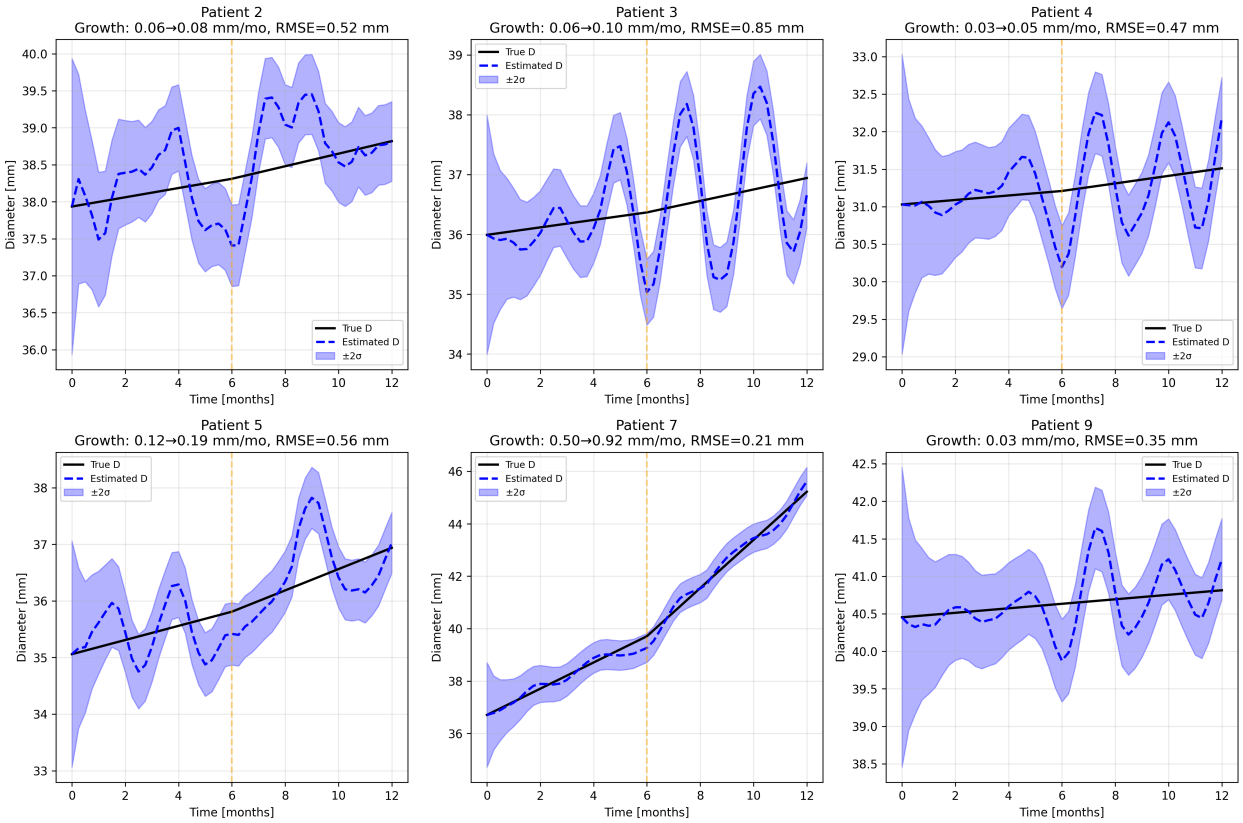


Figure 5: Diameter tracking using imperfectly calibrated patient-specific parameters. Six representative patients are shown with varying growth patterns. Black solid lines: true diameter; blue dashed lines: estimated diameter; blue shading: $\pm 2\sigma$ uncertainty; orange vertical lines: growth acceleration timepoints where applicable. Despite parameter estimation errors, tracking RMSE remains below 1 mm for most patients. Note that y-axis are scaled differently for each plot to highlight differences from true diameter trajectories.

Importantly, the tracking validation with imperfect calibration demonstrates that not all parameters require accurate estimation. The system exhibits robustness to certain parameter errors, suggesting that the combination of parameters most relevant to diameter sensitivity can be adequately characterized even when individual parameters are poorly constrained. Future work should investigate minimal calibration protocols that identify only the critical parameter combinations.

### 4.5. Clinical Translation Considerations

Several factors must be addressed for clinical translation. First, real PPG signals contain motion artifacts, varying skin contact, and environmental interference not present in our idealized simulations. Signal quality assessment and artifact rejection will be essential preprocessing steps. Second, our model assumes AAA location is known from initial imaging; detecting de novo aneurysms or aneurysms at atypical locations would require additional approaches. Third, the calibration procedure assumes access to clinical-grade diameter, HR, and MAP measurements; streamlined protocols using only imaging diameter plus PPG-derived HR and blood pressure estimates merit investigation.

The proposed workflow envisions PPG monitoring as a complement to, not replacement for, periodic imaging. Clinical imaging would provide ground-truth diameter measurements and re-calibration

opportunities, while continuous PPG monitoring would interpolate between visits and flag unexpected changes for earlier follow-up.

### 4.6. Limitations

This study has several limitations. First, the hemodynamic model, while physics-based, is a simplified 1D representation that omits three-dimensional flow features, vessel curvature, and branch effects. More sophisticated models (e.g., 3D-0D coupled simulations) would provide higher fidelity at increased computational cost. Second, the neural surrogate, while accurate on the training distribution, may exhibit degraded performance for parameter combinations outside the training range. Third, the tracking simulations assume stationary noise characteristics; real wearable data quality varies with activity, posture, and device adherence. Fourth, we have not validated against clinical data; the simulated patients and growth patterns, while physiologically motivated, may not capture the full complexity of real AAA progression.

## 5. Conclusion

We have demonstrated through computational analysis that continuous PPG monitoring could enable tracking of aortic aneurysm diameter between clinical imaging appointments. While single observations are fundamentally limited by poor identifiability (condition number $\kappa \approx 740$), aggregating thousands of measurements under varying physiological conditions achieves sub-millimeter precision according to Cramér-Rao bounds. Bayesian sequential estimation successfully tracks simulated aneurysm growth over 12 months, including scenarios with growth acceleration, with RMSE consistently below 0.35 mm. The framework demonstrates robustness to imperfect patient-specific model calibration, maintaining median tracking RMSE of 0.49 mm across 50 virtual patients.

These results suggest that wearable PPG monitoring warrants further investigation as a complementary surveillance modality for aortic aneurysm patients. Clinical validation studies correlating PPG-derived features with imaging-confirmed diameter changes are needed to translate these theoretical findings toward practical application.

## Acknowledgments

Acknowledgments go here *but should only appear in the camera-ready version of the paper if it is accepted*. Acknowledgments do not count toward the paper page limit.

## References

H Thomas Banks, Shuhua Hu, and W Clayton Thompson. Modeling and inverse problems in the presence of uncertainty. *CRC Press*, 2014.

Peter H Charlton, Vaidotas Marozas, et al. Wearable photoplethysmography for cardiovascular monitoring. *Proceedings of the IEEE*, 110(3):355–381, 2022.

John A Elefteriades. Thoracic aortic aneurysm: reading the enemy's playbook. *Current problems in cardiology*, 33(5):203–277, 2008.

Mohamed Elgendi. On the analysis of fingertip photoplethysmogram signals. *Current Cardiology Reviews*, 8(1):14–25, 2012.

K Craig Kent, Robert M Zwolak, Natalia N Egorova, Thomas S Riles, Andrew Manganaro, Alan J Moskowitz, Annetine C Gelijns, and Giampaolo Greco. Analysis of risk factors for abdominal aortic aneurysm in a cohort of more than 3 million individuals. *Journal of Vascular Surgery*, 59(6): 1450–1458, 2014.

Sandrine C Millasseau, Ronan P Kelly, James M Ritter, and Philip J Chowienczyk. Contour analysis of the photoplethysmographic pulse measured at the finger. *Journal of Hypertension*, 24(8):1449–1456, 2006.

Ramakrishna Mukkamala, Jin-Oh Hahn, Omer T Inan, Lalit K Mestha, Chang-Sei Kim, Hakan Töreyin, and Survi Kyal. Toward ubiquitous blood pressure monitoring via pulse transit time: theory and practice. *IEEE Transactions on Biomedical Engineering*, 62(8):1879–1901, 2015.

Wilmer W Nichols, Michael F O'Rourke, and Charalambos Vlachopoulos. Mcdonald's blood flow in arteries: Theoretical, experimental and clinical principles. *CRC Press*, 2011.

Jorg J Reimerink, Maarten J van der Laan, Mark J Koelemay, Ron Balm, and Dink A Legemate. Systematic review and meta-analysis of population-based mortality from ruptured abdominal aortic aneurysm. *British Journal of Surgery*, 100(11): 1405–1413, 2013.

Natzi Sakalihasan, Jean-Baptiste Michel, Athanasios Katsargyris, Helena Kuivaniemi, Jean-Olivier Defraigne, Alain Nchimi, Janet T Powell, Koichi Yoshimura, and Rebecka Hultgren. Abdominal aortic aneurysms. *Nature Reviews Disease Primers*, 4(1):1–22, 2018.

Fabian Schrumpf, Patrick Frenzel, Christoph Aust, Georg Osterhoff, and Mirco Fuchs. Assessment of non-invasive blood pressure prediction from ppg and rppg signals using deep learning. *Sensors*, 21 (18):6022, 2021.

Simon G Thompson, Heather A Ashton, Lei Gao, and Rodney AP Scott. Screening for abdominal aortic aneurysm: a systematic review for the us preventive services task force. *Annals of Internal Medicine*, 144(3):203–208, 2002.

## Appendix A. PPG Waveform Generation

Figure 6 in the main text demonstrates the physiological realism of simulated PPG waveforms. The model produces characteristic features observed in clinical PPG recordings: a rapid systolic upstroke reflecting the arrival of the pulse wave, a systolic peak followed by a brief notch (the dicrotic notch, representing aortic valve closure), and an exponential diastolic decay. As mean arterial pressure increases, the waveforms show expected changes including altered pulse pressure and modified dicrotic notch prominence.

## Appendix B. Neural Surrogate Performance

Table 3 provides detailed validation metrics for the neural surrogate model.

Note: MAPE is not reported for AI due to values near zero causing numerical instability.

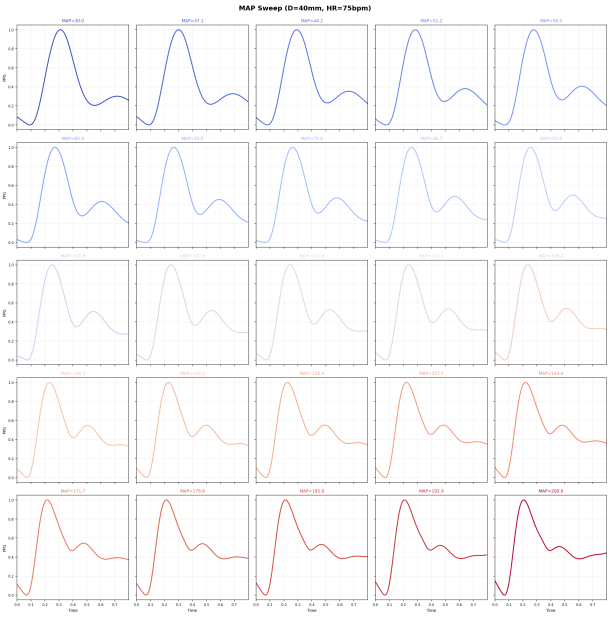


Figure 6: Simulated PPG waveforms at the digital artery across a range of mean arterial pressures (30–200 mmHg) at fixed diameter (40 mm) and heart rate (75 bpm). Waveforms demonstrate physiologically realistic features including systolic peak, dicrotic notch, and diastolic decay. Color progression from blue (low MAP) to red (high MAP) illustrates systematic changes in waveform morphology with blood pressure.

Table 3: Neural surrogate validation performance on held-out test set.

| Feature | RMSE | MAE | $R^2$ | MAPE (%) |
|---|---|---|---|---|
| PTT (ms) | 5.22 | 2.57 | 0.76 | 5.0 |
| $\mathrm{PWV}_{\mathrm{eff}}$ (m/s) | 0.85 | 0.49 | 0.89 | 3.3 |
| AI | 0.057 | 0.024 | 0.89 | — |
| RI | 0.019 | 0.008 | 0.92 | 1.1 |
| SI (m/s) | 0.85 | 0.49 | 0.89 | 3.3 |
| $t_{\mathrm{sys}}$ ratio | 0.018 | 0.008 | 0.95 | 2.4 |
| DN timing (ms) | 13.2 | 7.1 | 0.89 | 3.4 |

## Appendix C. Justification for MAP Measurement Uncertainty

We assumed $\sigma_{\mathrm{MAP}} = 10$ mmHg for blood pressure estimation from PPG signals. This value is consistent with recent literature on cuff-less blood pressure monitoring. Mukkamala et al. (2015) reported that PTT-based methods achieve approximately 8–12 mmHg error for systolic BP in controlled settings. Schrumpf et al. (2021) found mean absolute errors of 7–15 mmHg for various PPG-based estimation approaches. We selected 10 mmHg as a representative value for current wearable technology, acknowledging that accuracy may improve with advances in calibration methods and sensor quality.